International Journal of Thermal Sciences 136 (2019) 337–346

Contents lists available at ScienceDirect

International Journal of Thermal Sciences

journal homepage: www.elsevier.com/locate/ijts

A Bi-Layer compact thermal model for uniform chip temperature control with non-uniform heat sources by genetic-algorithm optimized microchannel cooling

Ruikang Wu, Xinfeng Zhang, Yiwen Fan, Run Hu, Xiaobing Luo*

State Key Laboratory of Coal Combustion, School of Energy and Power Engineering, Huazhong University of Science and Technology, Wuhan, 430074, China

ARTICLE INFO

Keywords:
Non-uniform
Microchannel
Genetic algorithm
Compact thermal model
Hot-spot
Liquid cooling

ABSTRACT

Due to the difference of local power in semiconductor chips, the chip temperature is usually non-uniform with hot spots, which may cause problems like thermal stress and interfacial delamination, thus deteriorating the reliability and decreasing the electrical performance. Therefore, uniform chip temperature is demanded and pursued both by both industry and academics. The most commonly used single-phase microchannel liquid cooling is efficient but suffered from severe temperature non-uniformity, which may be tackled by tuning local channel densities. However, the existing one-dimensional model is not enough for the channel density design of microchannel with non-uniform heat flux, for it's lack of the description of heat spreading effect. In this study, we presented a bi-layer compact thermal model with considering the three-dimensional heat spreading and thermal conduction for the junction temperature gradient prediction in microchannels with non-uniform heat source. This analytical model accurately predicts the junction temperature gradient with error within 4.8% compared with COMSOL simulation results. Combining the present model with genetic algorithm, we designed a microchannel with optimized local channel widths to achieve the temperature uniformity as high as ~90%. The maximum junction surface temperature difference is reduced from 45 °C to 13 °C with the existence of hot-spot with heat flux density of 200W/cm^2. The present model and design strategy can be used to diminish the hot spot and achieve uniform temperature in high-power chips for extensive applications like integrated circuits, IGBT, HEMT, etc.

1. Introduction

Semiconductor chips are recognized as the heart of advanced technologies such as communications, light emitting diodes, high-performance computers and mobile devices [1–4]. Driven by Moore's law, the number of internal transistors of the latest Core series has reached 580 million [5], resulting in high heat flux density and high chip temperature. Starting with the seminal work of Tuckerman and Pease [6], single-phase microchannel liquid cooling, which has the heat dissipation capability of heat flux up to 790W/cm^2, has been widely investigated and applied to cool the chips [7–11]. In the past decades, most researches on microchannel liquid cooling focused on maintaining the maximum junction temperature under a critical value, regardless of the temperature uniformity [12–15]. However, due to the different thermal expansion coefficient (CTE), large temperature gradient increases the thermal stress in the chip and even cause interfacial delamination, resulting in performance degradation and low reliability [16]. On the other hand, single-phase microchannel liquid cooling usually has uniform heat dissipation capability, which means that when hotspots are kept under critical temperature, the other places (backgrounds) along the straight channels may be subcooled, resulted as a waste of energy [17]. For example, it is investigated that roughly 33% of the total electricity consumed is allocated to thermal management systems of server electronics [18]. Temperature gradient is not only caused by non-uniform heat source, but also by temperature rise of the flowing fluid in microchannel, which is the inherent disadvantage of single-phase liquid cooling.

Recently, extensive researches have been done to solve the temperature uniformity problem including two-phase flow boiling and single-phase microchannel liquid cooling with various local channel densities. Although two-phase flow boiling presents much larger heat dissipation capability, the instability and critical heat flux problem are hard to handle and is still far from industrial application [19–22]. Luo et al. designed a tree-like microchannel to deal with temperature

* Corresponding author.
E-mail address: luoxb@hust.edu.cn (X. Luo).

https://doi.org/10.1016/j.ijthermalsci.2018.10.047
Received 11 June 2018; Received in revised form 23 September 2018; Accepted 30 October 2018

uniformity of multiple heat sources [16], and the temperature difference can be controlled within 1.3 °C. Lorenzini et al. used microgaps with variable pin fin clustering in the microchannel and had a great cooling effect on the hotspot with high heat flux [23]. Sharma et al. used the manifold microchannel with alternately fine and coarse channels to cool the electronics with multiple heat sources [24]. Although locally fine channels can provide larger local heat transfer capability owing to the larger heat transfer area, the flow rate may decrease due to the larger flow resistance and maldistribution effect, on the contrary, resulting in higher surface temperature. So the structure of the microchannel, such as how wide the local channel is, has a significant influence on the surface temperature that can not be simply described by experiences. Therefore, an accurate model and optimal method are urgently required for the microchannel structural design.

One dimensional (1D) thermal resistance model has been developed to predict the microchannel junction temperature. Most researches only considered the average surface temperature [25,26], regardless of the temperature gradient. Mao et al. developed a compact thermal model for microchannel substrate with high temperature uniformity subjected to multiple heat sources [27]. Sharma et al. proposed a hotspot-targeted semi-empirical design method, considering the temperature rise caused by heated fluid along the flowing direction [28]. However, the three-dimensional (3D) thermal conduction and heat spreading effect are not taken into account in the 1D model, thus temperature uniformity in the 1D model is not satisfied and far from the industry requirement. In this work, we presented a bi-layer compact microchannel thermal model with non-uniform heat sources that considered the 3D thermal conduction from the heat source to microchannel and the 1D thermal resistance model of the microchannel with fluid temperature rise taken into account. The modelling process is introduced with validation by COMSOL software, and based on the model we designed a microchannel with varying channel width to achieve uniform chip temperature.

2. Bi-layer compact thermal model

Fig. 1(a) shows the structure of a typical plate-fin microchannel with non-uniform heat source. Cold fluid enters the microchannel and flows along the channels. Heat generated by non-uniform heat source is conducted and diffused in the solid layer and then absorbed by fluid. The heated fluid flows out of the microchannel and carries the heat away. Based on the heat transfer process, the compact thermal model is composed of two parts. One is the 3D thermal conduction model that describes the heat conduction in the solid layer [29]. The other is the 1D thermal resistance model considering fluid temperature rise [28] that describes the heat transfer to fluid in the so-called convection layer.

2.1. Heat transfer in the solid layer

Heat conduction process in the solid layer is described by solving the 3D thermal conduction partial differential equation. Fig. 1(b) shows some of the required parameters of the model and the heat transfer process in the solid layer. The length and width of the microchannel are a and b, respectively. The thickness of the solid layer is t. The top surface is the chip heat source with non-uniform heat flux, and is described as $Q(x,y)$. The bottom surface is cooled by convection layer with an effective heat transfer coefficient of $h(x,y)$. The thermal conductivity of the microchannel material is k. The governing energy equation for the temperature field $T(x,y,z)$ is given by

$$\frac{\partial^2 T}{\partial x^2} + \frac{\partial^2 T}{\partial y^2} + \frac{\partial^2 T}{\partial z^2} = 0 \tag{1}$$

with the following boundary conditions described as

$$\frac{\partial T}{\partial x}|_{x=0,a} = 0 \tag{2}$$

$$\frac{\partial T}{\partial y}|_{y=0,b} = 0 \tag{3}$$

$$k\frac{\partial T}{\partial z}|_{z=0} + Q(x, y) = 0 \tag{4}$$

$$k\frac{\partial T}{\partial z}|_{z=t} + h(x, y)(T(x, y, t) - T_{fluid,in}) = 0 \tag{5}$$

where $T_{fluid,in}$ is the inlet fluid temperature as shown in Fig. 1(c). The

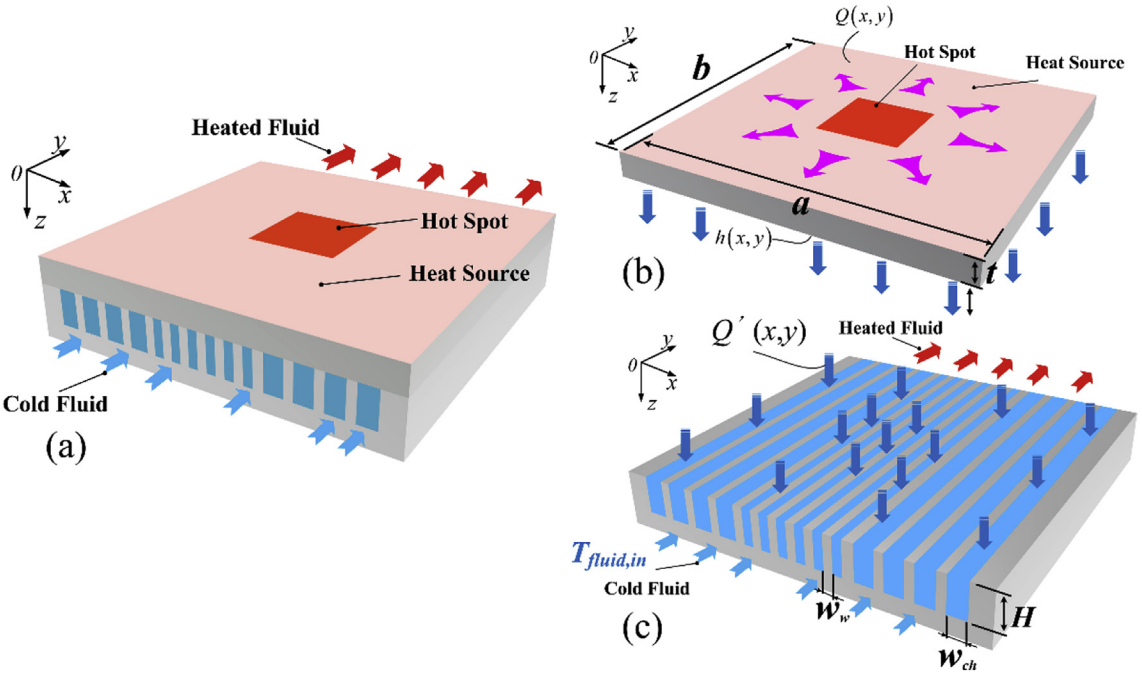

Fig. 1. Schematic diagram of (a) a typical plate-fin microchannel with non-uniform heat source (b) structure and the heat transfer process of the solid layer (c) structure, heat transfer process and the fluid flow of the convection layer.

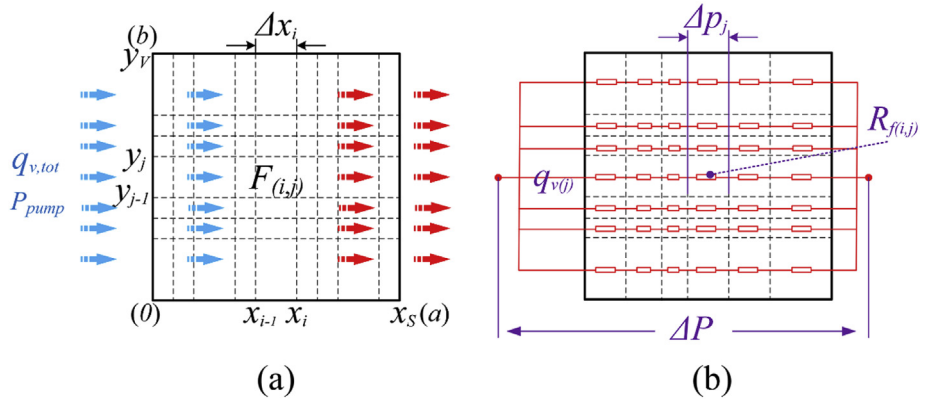

Fig. 2. Schematic diagram of (a) the discretization of the computational domain (b) the flow resistance network of the discrete convection layer.

effective heat transfer coefficient $h(x,y)$ describes the heat transfer from the bottom surface of the solid layer to the heat sink with temperature $T_{fluid,in}$, which is the cold source of the microchannel. To solve the above equations, temperature field can be written as the two-variable Fourier series and derived as the flowing equation

$$T(x,y,z) = \left(A_{00} - \frac{U_{00}}{k_z}z\right) + \sum_{n=0}^{N}\sum_{m=0}^{M}\left(\begin{matrix}A_{nm}(\exp(\lambda_{nm}z) + \exp(-\lambda_{nm}z)) \\ +\frac{U_{nm}}{\lambda_{nm}k}\exp(-\lambda_{nm}z)\end{matrix}\right)\cos\left(\frac{n\pi x}{a}\right)\cos\left(\frac{m\pi x}{b}\right) \tag{6}$$

where

$$U_{00} = \frac{1}{ab}\int_0^b\int_0^a Q(x,y)dxdy \tag{7}$$

$$U_{nm} = \frac{\varepsilon_{nm}}{ab}\int_0^b\int_0^a Q(x,y)\cos\left(\frac{n\pi x}{a}\right)\cos\left(\frac{m\pi y}{b}\right)dxdy \tag{8}$$

$$\varepsilon_{nm} = \begin{cases}2 & n=0 \text{ or } m=0\\ 4 & n\neq 0,\ m\neq 0\end{cases} \tag{9}$$

$$\lambda_{nm} = \sqrt{\left(\frac{n\pi}{a}\right)^2 + \left(\frac{m\pi}{b}\right)^2} \tag{10}$$

and the parameters A_{00} and A_{nm} satisfy the following group of equations

$$\begin{aligned}&A_{00}\int_0^b\int_0^a h(x,y)dxdy \\ &+\sum_{n=0}^{N}\sum_{m=0}^{M}A_{nm}(\exp(\lambda_{nm}t) \\ &\quad+\exp(-\lambda_{nm}t))\int_0^b\int_0^a h(x,y)\cos\left(\frac{n\pi x}{a}\right)\cos\left(\frac{m\pi y}{b}\right)dxdy \\ &= U_{00}ab + U_{00}\frac{t}{k}\int_0^b\int_0^a h(x,y)dxdy \\ &-\sum_{n=0}^{N}\sum_{m=0}^{M}\frac{U_{nm}}{k\lambda_{nm}}\exp(-\lambda_{nm}t)\int_0^b\int_0^a h(x,y)\cos\left(\frac{n\pi x}{a}\right)\cos\left(\frac{m\pi y}{b}\right)dxdy\end{aligned} \tag{11}$$

$$A_{00}d_{ij} + A_{ij}e_{ij} + \sum_{n=0}^{N}\sum_{m=0}^{M}A_{nm}f_{ijnm} = U_{00}g_{ij} + U_{ij}l_{ij} + \sum_{n=0}^{N}\sum_{m=0}^{M}U_{nm}S_{ijnm} \tag{12}$$

where

$$d_{ij} = \int_0^a\int_0^b h(x,y)\cos\left(\frac{i\pi x}{a}\right)\cos\left(\frac{j\pi y}{b}\right)dxdy \tag{13}$$

$$e_{ij} = k\lambda_{ij}(\exp(\lambda_{ij}t) - \exp(-\lambda_{ij}t))N_{x,i}N_{y,j} \tag{14}$$

$$\begin{aligned}f_{ijnm} &= (\exp(\lambda_{nm}t) + \exp(-\lambda_{nm}t))\int_0^a\int_0^b h(x,y) \\ &\times\cos\left(\frac{n\pi x}{a}\right)\cos\left(\frac{m\pi x}{b}\right)\cos\left(\frac{i\pi x}{a}\right)\cos\left(\frac{j\pi x}{a}\right)dxdy\end{aligned} \tag{15}$$

$$g_{i,j} = \frac{t}{k}f_{ij} \tag{16}$$

$$l_{ij} = \exp(-\lambda_{nm}t)N_{x,i}N_{y,j} \tag{17}$$

$$S_{ijnm} = \frac{-\exp(-\lambda_{nm}t)}{k\lambda_{nm}(\exp(\lambda_{nm}t) + \exp(-\lambda_{nm}t))}f_{ijnm} \tag{18}$$

$$N_{x,i} = \begin{cases}a & i=0\\ a/2 & i\neq 0\end{cases},\quad N_{y,j} = \begin{cases}b & j=0\\ b/2 & j\neq 0\end{cases} \tag{19}$$

where $i = 0,1,2,\ldots,N$ and $j = 0,1,2,\ldots,M$, while i and j can not be zero at the same time. The upper limits of Fourier series are set to be $n = N$ and $m = M$ for computation. It should be noted that, in all equations in this section, n and m can not be both zero at the same time. According to Eqs. (11) and (12), there is a set of $(N+1) \times (M+1)$ linear equations in $(N+1) \times (M+1)$ variables, with unknown parameters A_{00},A_{01},A_{02}, …,A_{NM}. This set of equations can be solved by matrix inversion using the Matlab. Then the temperature field may be obtained. Details about the derivation of the above equations may refer to these works [29–31].

The heat transfer coefficient of the bottom surface is related to the total thermal resistance $R_{total}(x,y)$ of the convection layer according to energy conservation, satisfying

$$h(x,y)(T(x,y,t) - T_{fluid,in}) = \frac{T(x,y,t) - T_{fluid,in}}{R_{total}(x,y)}. \tag{20}$$

2.2. Heat transfer in the convection layer

Fig. 1(c) shows the structure of the convection layer, in which $Q'(x,y)$ is the input heat flux from the solid layer. W_{ch}, W_w and H are the channel width, channel wall width and channel height, respectively. In general, the heat flux, channel width and channel wall may all be non-uniformly distributed. Therefore, the computational domain must be discretized (Fig. 2(a)) such that each cell of the discretized domain encompasses an area of nearly constant quantity $F(i,j)$. More specifically, $F(i,j)$ may represent $Q'(i,j)$, $R_{total}(i,j)$, $w_{ch}(i,j)$, $w_w(i,j)$, etc. It should be noted that, it is assumed that the heat transfer is 1D from the bottom surface of the solid layer to the fluid in the relevant channel of the same discrete cell. And the heat transfer between channels in y-direction is ignored.

Fig. 2(a) shows the flow direction, and the average coolant temperature in the (i,j)th cell is calculate according to energy conservation and is given by

$$T_{fluid}(i,j) = T_{fluid,in} + \sum_{k=1}^{i-1}\frac{Q'(k,j)\Delta x_k\Delta y_j}{\rho q_v(j)c_p} + \frac{Q'(i,j)\Delta x_i\Delta y_j}{2\rho q_v(j)c_p} \tag{21}$$

where $q_v(j)$ represents the volume flow rate in the jth line and c_p is the fluid heat capacity. The number of discrete mesh in x-direction and y-

direction is S and V, respectively. So the total input volume flow rate should be $q_{v,tot} = \sum_{j=1}^{V} q_v(j)$. Fig. 2(b) shows that, in analogy with the Ohm's law in circuitry, volume flow rate of each line satisfies the following equation

$$q_v(j) = \frac{\Delta P}{\sum_{k=1}^{S} R_f(i,j)} \tag{22}$$

where ΔP represents the total pressure loss of the microchannel. $R_f(i,j)$ represents the flow resistance in the (i,j)th cell and is described as follows:

$$R_f(i,j) = \frac{2\mu_f (f\,\mathrm{Re})_{(i,j)} (w_{ch}(i,j) + w_w(i,j))\Delta x_i}{D_{ch}^2(i,j) w_{ch}(i,j) H \Delta y_j} \tag{23}$$

where $D_{ch}(i,j) = 2w_{ch}(i,j)\mathrm{H}/(w_{ch} + \mathrm{H})$ represents the local equivalent hydraulic diameter. In the calculation, at least one input quantity ($q_{v,tot}$, ΔP *and* input pumping power P_{pump}) should be known. In this work, we care more about the energy consumption, so we set the pumping power as the known constant input parameter and it satisfies the relationship $P_{pump} = \Delta P \cdot q_{v,tot}$. It can be seen from Eq. (21)–(23) that the fluid temperature and the flow resistance are only dependent on the microchannel structure and the input heat flux.

Fig. 3 shows the thermal resistance model of the convection layer. According to the thermal resistant network, the thermal resistances can be calculated by

$$R_{tot}(i,j) = R_{fth}(i,j) + \left(\frac{1}{R_{fconv}(i,j)} + \frac{1}{R_{wcond}(i,j) + R_{wconv}(i,j)} \right)^{-1} \tag{24}$$

where R_{fth}, R_{fconv}, R_{wcond}, R_{wconv} represent the effective fluid thermal resistance, fluid convection thermal resistance, conduction thermal resistance to the wall and the wall conduction thermal resistance, respectively. The resistances are given by

$$R_{fth}(i,j) = \frac{T_{fluid}(i,j) - T_{fluid,in}}{Q'(i,j)} \tag{25}$$

$$R_{fconv}(i,j) = \frac{w_{ch}(i,j) + w_w(i,j)}{h_f(i,j) w_{ch}(i,j)} \tag{26}$$

$$R_{wcond}(i,j) + R_{wconv}(i,j) = \frac{w_{ch}(i,j) + w_w(i,j)}{2h_f(i,j) H \gamma(i,j)} \tag{27}$$

where γ is the fin efficiency [28] and h_f is the convection heat transfer coefficient of the flowing fluid which is given by $h_f(i,j) = Nu_D(i,j)k_f/D_{ch}(i,j)$. k_f is the thermal conductivity of the fluid. Flow in the microchannel is usually laminar [32] because of the small hydraulic diameter. It is assumed to be fully developed and the relations for Nu and fRe in Eq. (23) are adopted from Shah [33].

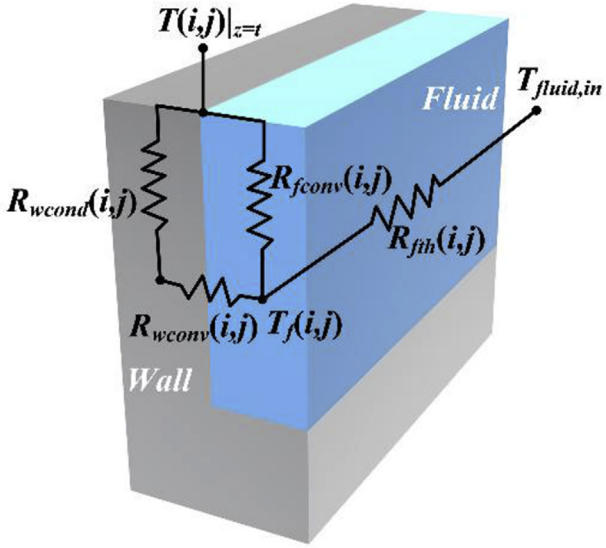

Fig. 3. Thermal resistance model of the convection layer.

2.3. Heat flux iteration

Resulting from the heat spreading in the solid layer, heat flux distribution $Q'(x,y)$ is different from $Q(x,y)$ and is unknown. Solving the 3D heat conduction partial differential equation requires the effective heat transfer coefficient h of the bottom surface to be known. However, h cannot be obtained unless $Q'(x,y)$ is known, according to the above mentioned in section 2.2. Therefore, solving $Q'(x,y)$ is the key for the bi-layer compact thermal model. Combining the 3D heat conduction model in the solid layer with the 1D thermal resistance model, the bottom surface temperature field of the solid layer can be solved by $T(x,y,t) = f(Q'(x,y))$ and h is obtained by $h = g(Q'(x,y))$. In addition, at the interface of two layers, the heat flux of the bottom surface of the solid layer and $Q'(x,y)$ must be equal. Thus we have

$$\begin{aligned} Q'(x,y) &= h[T(x,y,t) - T_{fluid,in}] \\ &= g(Q'(x,y))[f(Q'(x,y)) - T_{fluid,in}] \end{aligned} \tag{28}$$

Eq. (28) shows that $Q'(x,y)$ is the fixed point matrix and we can solve it by iteration. Fig. 4 shows the flow chart of the iteration process. The initiate value should be $Q(x,y)$. ε represents the error and we set it to be 0.01 for computation.

3. Genetic algorithm optimization

When the pumping power is set to be constant, we believe that the optimum microchannel structure is to make the junction surface temperature uniform. By regulating the local channel width and wall width, it is able to change the local flowrate and heat transfer coefficient, and eventually reaches the best temperature uniformity. The genetic algorithm (GA) is invoked to do the optimization. It is a semi-stochastic global search method, based on an analogy with Darwin's laws of natural selection. The GA generally consists of the population initialization, selection, crossover, and mutation processes [34]. The selection rule in this work is set as the standard deviation of the temperature field which is given by

$$\begin{aligned} &\min\left(\sqrt{\frac{\sum (T - \overline{T})^2}{N_{Tx} N_{Ty} - 1}} \right) \\ &= \min f(w_{ch}(1,1), w_{ch}(1,2), \ldots, w_{ch}(S,V), w_w(1,1), w_w(1,2), \ldots, w_w(S,V)) \end{aligned} \tag{29}$$

where $\overline{T}$ is the average junction surface temperature. N_{Tx} and N_{Ty} are the x- and y-direction discrete numbers of the surface temperature gradient, respectively. The GA in this work is aimed at finding the chrome that has the minimum standard deviation. And confinements of variables are as follows

$$w_{ch,\min} \le w_{ch}(i,j) \le w_{ch,\max} \qquad i = 1,2,\ldots,S \;\; j = 1,2,\ldots,V \tag{30}$$

$$w_{w,\min} \le w_w(i,j) \le w_{w,\max} \qquad i = 1,2,\ldots,S \;\; j = 1,2,\ldots,V \tag{31}$$

4. Results and discussion

In this work, the bi-layer compact thermal model was coded using the Matlab and was verified by the COMSOL simulation. As the flow and heat transfer in the plate-fin microchannel are not that complex, the coupled CFD and Heat Transfer package in COMSOL MULTIPHYSICS is accurate enough for the simulation [35]. The calculated chip microchannel structure parameters and material physical properties are listed in Table 1. The material of the chip microchannel is silicon and water is selected as the cooling fluid. Considering the fabrication

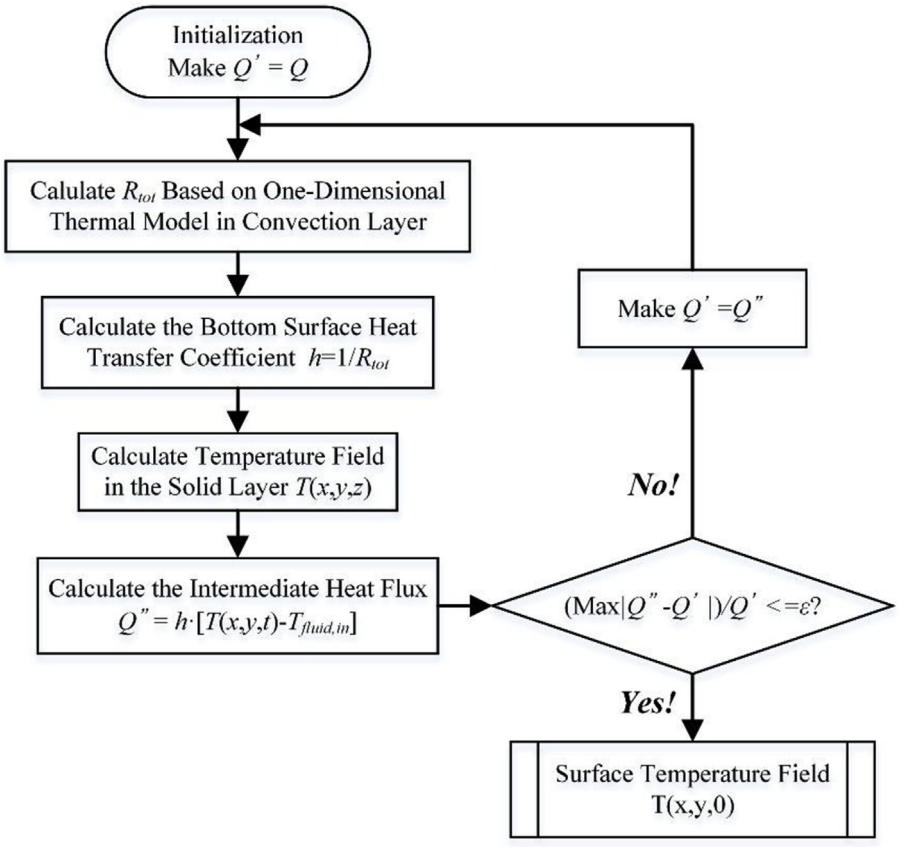

Fig. 4. Flow chart of the heat flux iteration process of the bi-layer compact thermal model.

Table 1
Microchannel structure and physical property parameters.

$a \times b$ (mm)		t (μm)	W_w (μm)		H (μm)
12 × 16		225	30		300
material	k (W/m·K)	ρ (kg/m3)	μ (Pa·s)	c_p (J/Kg·K)	$T_{fluid,in}$ (°C)
water	0.599	998.2	0.001	4180	20
silicon	150	/	/	/	/

complexity, the channel wall width is set to be constant and uniform.

In order to verify the bi-layer compact thermal model, three cases with various channel distribution and heat source distribution are compared. Case A represents the simplest condition that the heat source and channel distribution are both uniform. Case B represents microchannel with uniform channel distribution and non-uniform heat source. Case C represents microchannel with non-uniform channel distribution and heat source. The specific parameters of case A, B and C are listed in Table 2. For simplicity, the non-uniform heat source in this study is composed of a central hotspot with higher heat flux and a background with lower heat flux. However, it should be noted that, the bi-layer compact thermal model is also suitable for the heat source with multi-hotspots, because heat flux in this model is described by a function $Q(x,y)$.

Table 2
Heat source and channel width distribution for case A, B and C.

	Q (HS) W/cm^2	Q (BG) W/cm^2	w_{ch} (HS) μm	w_{ch} (BG) μm
Case A	100	100	80	80
Case B	200	66.6667	80	80
Case C	200	66.6667	50	80

Fig. 5 shows the surface temperature comparison between results from bi-layer model, COMSOL simulation and 1D model [28]. Results show that, for case A, the 1D model and the bi-layer compact thermal model can both predict the surface temperature accurately. However for case B and C, the bi-layer compact thermal model can still accurately predict the temperature contour, but the 1D model shows large discrepancy from the COMSOL simulation. This is owing to the fact that the 1D model is unable to describe the hotspot heat spreading from high temperature to low temperature in the solid layer. The Matlab code for the bi-layer compact thermal model only costs a few seconds, rather than several hours that required for the COMSOL simulation.

The assignment of heat sources in case A, B and C makes the average heat flux to be equal as 100W/cm^{2}and the total thermal power to be 192W. And the input cooling energy, namely the pumping power, is set to be constant as 0.015W. Fig. 6 shows the calculated surface temperature for case A, B and C, in which Line D represents the line $y = 8$ mm on the top surface and Line E represents the line $x = 9$ mm on the top surface. We can see that along the flow direction (x-direction), calculated results of bi-layer model and 1D model both fit well with that of the COMSOL simulation. However, the calculated results of 1D model along y-direction is not accurate. The maximum temperature discrepancy in Fig. 6 between the bi-layer thermal compact model and the COMSOL simulation is only 4.8%. The surface temperature rises along the flow direction because of the heat absorption of fluids. This is one of the main reason that causes the non-uniform temperature. Results in Fig. 6 show that, even the average heat flux keeps the same, surface temperature of case B and C are much larger than that of case A, indicating that the existence of hotspots with locally high heat flux will cause higher temperature. In addition, surface temperature of case C with locally fine channel is much higher than that of case A and B. This means that locally refined the channels might not help decreasing the

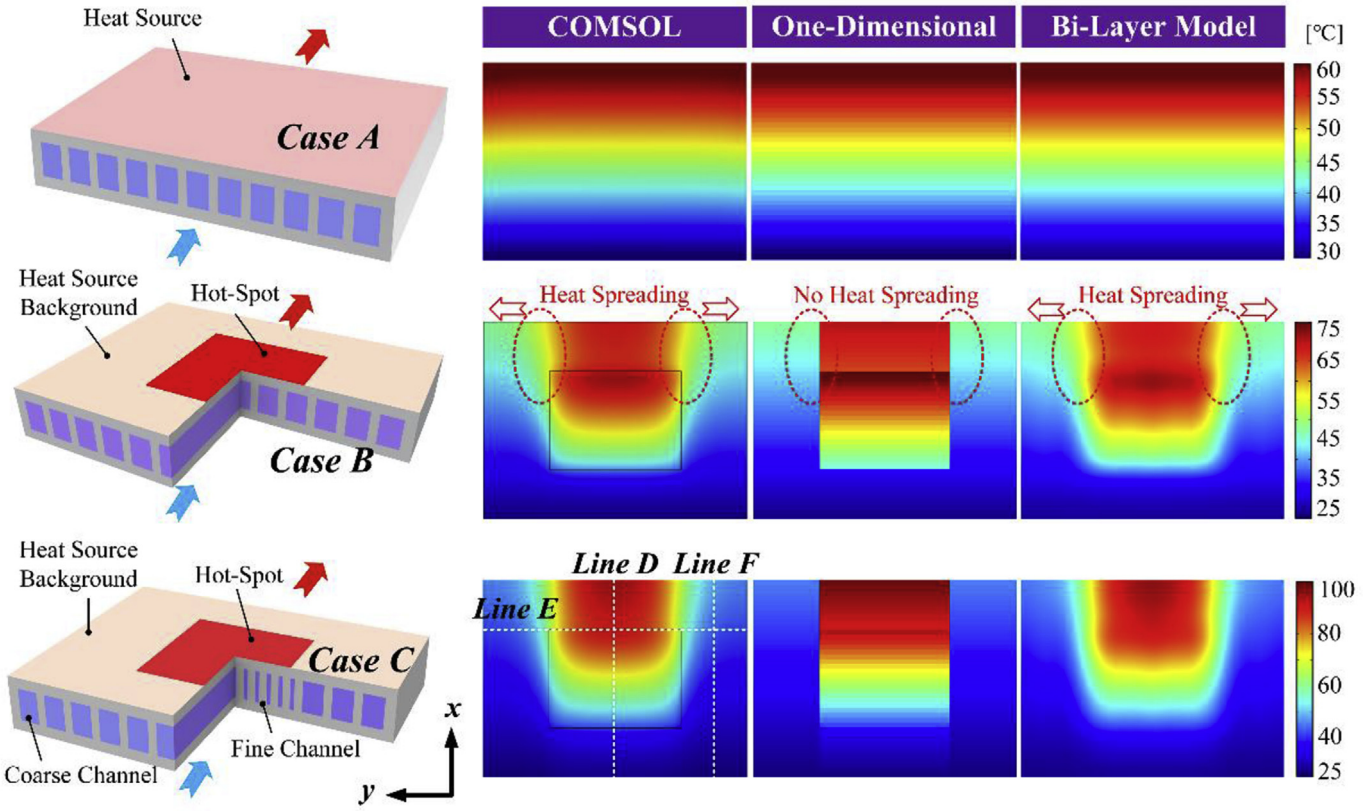

Fig. 5. Calculated junction surface temperature contour by COMSOL, 1D thermal resistance model and our bi-layer compact thermal model for case A, B and C.

temperature. On the contrary, it may weaken the cooling effect.

We can see clearly in Fig. 7 that this phenomenon is mainly caused by higher fluid temperature. Fig. 7 shows that the fluid temperature of case C is much larger than that of case B, which is caused by smaller flow rate in case C. As the fine channels in case C give rise to larger flow resistances, limited by the constant pumping power, the flow rate in case C should be the smallest among the three cases. What's more, the flow rate at the hotspot region is even much smaller because of the flow rate distribution. On the other hand, using the 1D theory, the surface temperature can be described as $T_{sur} = QR_{cond} + QR_{conv} + T_{fluid}$, where R_{cond} is the conduction thermal resistance of the solid layer and R_{conv} is the convection thermal resistance of the convection layer which is shown as the second term in Eq. (24). The solid layer structure and heat source of case B and C are nearly the same. The R_{conv} of case C is smaller than that of case B, owing to the larger heat transfer area of fine channels. Thus, the temperature difference ΔT_B is larger than ΔT_C. Therefore, the junction surface temperature gradient may be regulated by modifying the local channel structure, which is responsible for the change of the local R_{conv} and flow rate.

Fig. 8(a) shows the simulated pressure distribution for the case C at $z = 0.375$ cross section. The pressure distribution in the hotspot region is obviously different. It can be seen from Fig. 8(d) that the calculated pressure using the bi-layer model fits well with the COMSOL simulation and the flow resistance in the hotspot region is larger. Line F represents

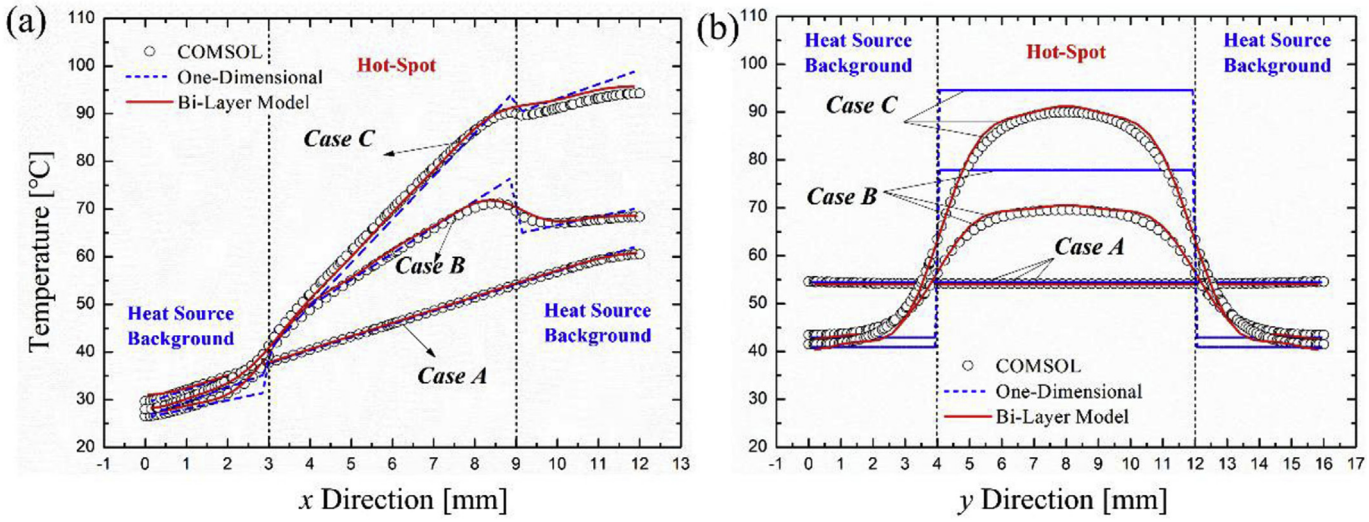

Fig. 6. Calculated surface temperature for case A, B and C of (a) line D ($y = 8$ mm) and (b) line E ($x = 9$ mm).

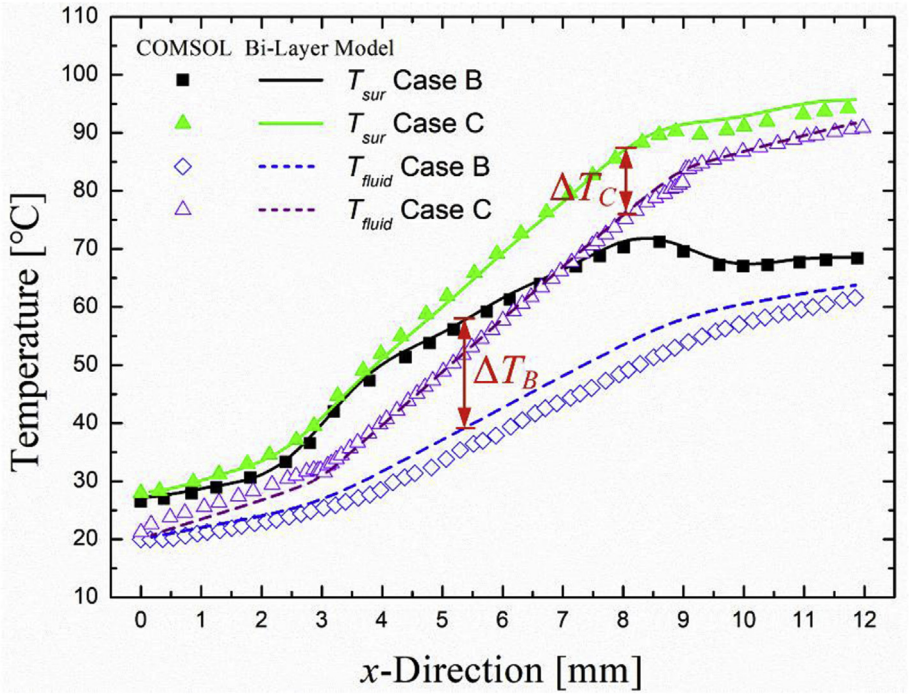

Fig. 7. Calculated surface temperature and fluid temperature along Line D for case B and C.

the line $y = 2$ in the cross section. Fig. 8(b) shows the simulated flow velocity. The maximum velocity is 0.85 m/s, so that the Reynolds number is less than 107.2, indication that it is laminar flow in the microchannel. The right side of Fig. 8(b) are upstream channels of the hotspot region and the left side are channels at background region. Because of the flow resistant difference, flow rate in the latter is apparently larger than that in the former. Fig. 8(c) shows the channel structure at the interface of fine and coarse channels. The distance between fine and coarse channel is set to be 50 μm for fabrication simplicity. It can be seen that fluid flows into the corresponding down stream channels without obvious vortex generated at the interface region.

The most important improvement of the bi-layer thermal compact model is that it uses the 3D heat conduction model to describe the heat spreading of the non-uniform heat source. Thus we verified this proposed model through changing the thickness of the solid layer *t*. Results

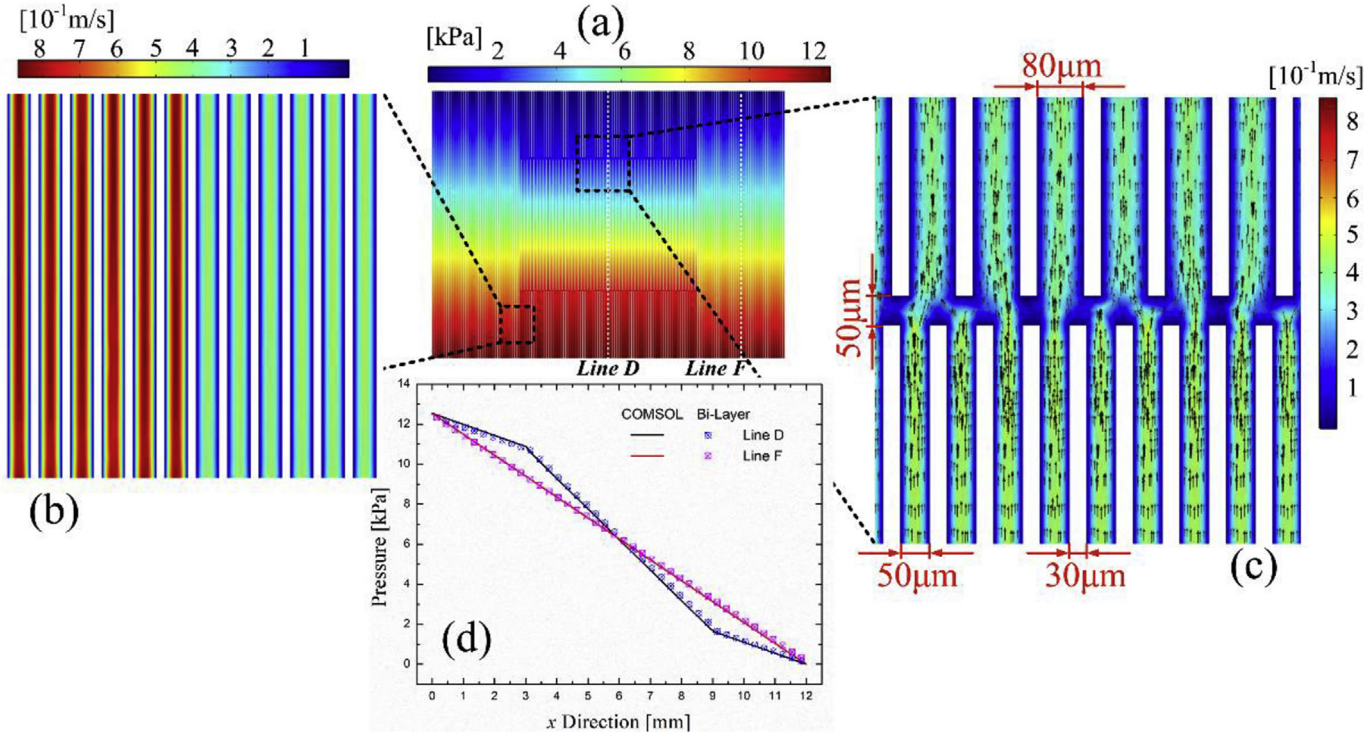

Fig. 8. (a) The pressure contour of the $z = 0.375$ mm cross section, (b) the flow velocity contour of the $z = 0.375$ mm cross section, (c) the streamline of the $z = 0.375$ mm cross section and (d) the pressure distribution along line D and line F.

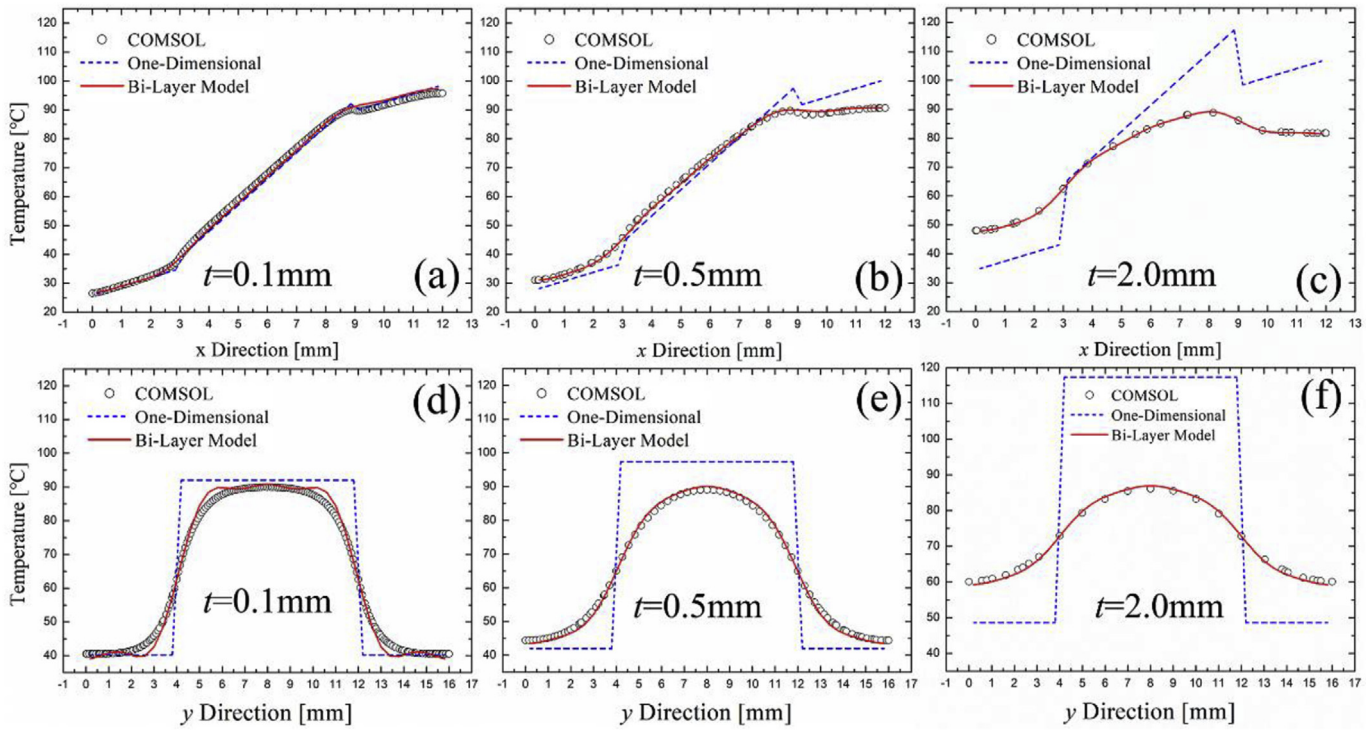

Fig. 9. Calculated surface temperature for case C of (a) line D (y = 8 mm) with t = 0.1 mm, (b) line D (y = 8 mm) with t = 0.5 mm, (c) line D (y = 8 mm) with t = 2 mm, (d) line E (x = 9 mm) with t = 0.1 mm, (e) line E (x = 9 mm) with t = 0.5 mm and (f) line E (x = 9 mm) with t = 2 mm.

in Fig. 9 (a)-(c) show that the bi-layer model predict the temperature accurately along the flow direction with t varying from 100 μm to 2 mm. But the 1D results shows huge discrepancies. Fig. 9 (d)-(f) show the same conclusion for the calculated temperature along the line E. When the solid layer thickness increases, the heat spreading of heat sources is more sufficient, so the 1D model can't properly predict the surface temperature gradient in this case.

In spite of the larger thermal conduction resistance induced by increasing the solid layer thickness, the temperature uniformity is better and the maximum temperature is reduced. Therefore, in the case when locally high heat flux exists, the heat spreading may be more important than heat conduction resistance. Therefore, the non-uniform microchannel design, to obtain a non-uniform local heat transfer coefficient, which results in the heat spreading effect, is very helpful to the temperature uniformity and hotspot cooling.

Fig. 10 (a) shows that when increase the channel width for case B, the maximum temperature first decreases to 69.72 °C, then increases to over 100 °C, regardless of the monotonically increasing flow rate. Fig. 10 (b) shows the maximum and minimum temperature varies with channel width at hotspot region with background channel width of 80 μm and 150 μm respectively. The best hotspot channel width for lowest maximum temperature and best uniformity is 90 μm for the case of background channel width with 80 μm and 100 μm for the case of background channel width with 150 μm. The flow rate and heat transfer coefficient corresponding to the channel width together determine the surface temperature gradient. So the channel width distribution optimization is required.

Considering a maximum feasible aspect ratio of 10 for microchannels [36] and the feasibility of the deep reactive ion etching technology, the silicon microchannel height H is assumed to be 300 μm

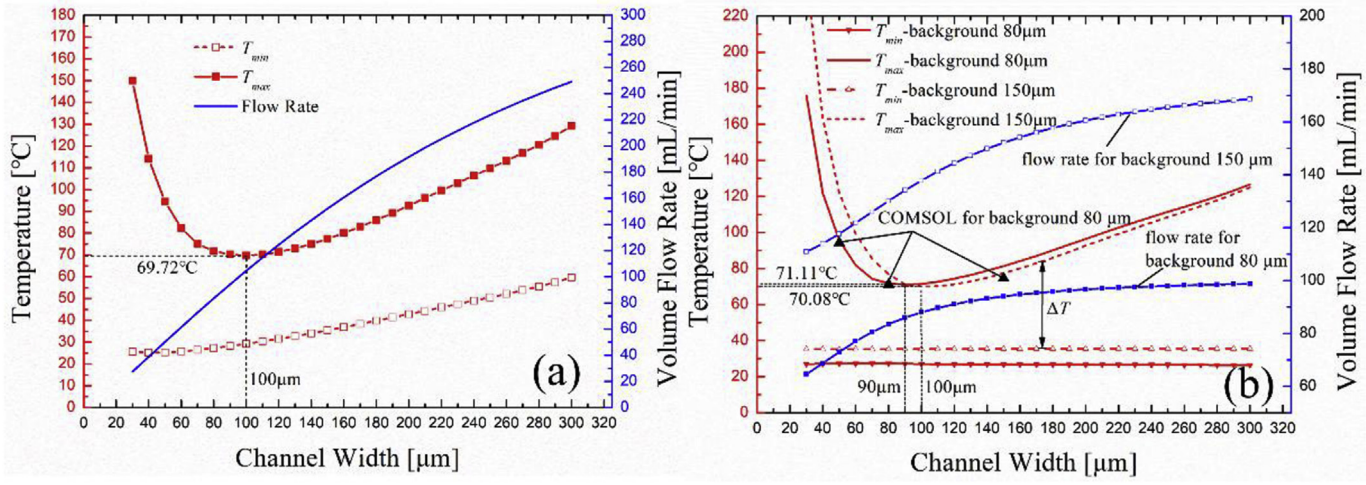

Fig. 10. Calculated maximum and minimum surface temperature with various channel width for (a) uniform channel like case B and (b) non-uniform channel like case C.

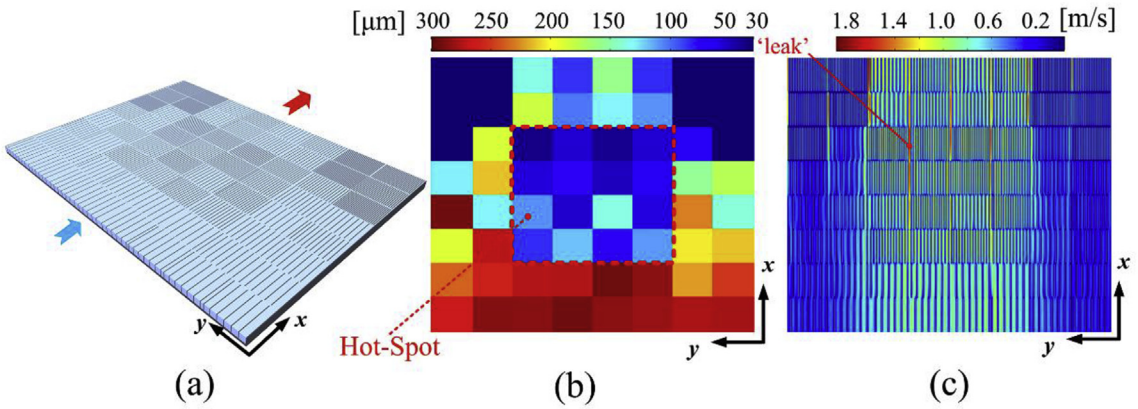

Fig. 11. (a) Structure of the optimized microchannel, (b) the optimized w_{ch} distribution for the microchannel and (c) the simulated fluid velocity distribution of the optimized microchannel at the z = 0.375 mm cross section.

and the channel width ranges from 30 μm to 300 μm. The channel wall width is set as a constant variable w_w. The inlet fluid temperature is 20 °C and the input pumping power is limited as 0.015W. The non-uniform heat source is set the same as case B.

Using the genetic algorithm described in Section 3, we obtained the microchannel structure with optimized channel distribution, which is shown in Fig. 11(a). The overall input volume low rate of the optimized microchannel is 95.1 mL/min. The channel wall width is optimized as 32 μm. Fig. 11(b) shows the optimized w_{ch} distribution for the microchannel. It can be observed that the w_{ch} gradually decreases along the flow direction in the background region, so that the temperature gradient along the flow direction caused by fluid temperature is as small as possible. Because large w_{ch} causes large convective thermal resistance, which makes up the low upstream fluid temperature. In addition, the w_{ch} of hot-spot is small to get large convective thermal resistance. The w_{ch} distribution makes a large aspect ratio of flow rate in the hot-spot region, to provide an enough heat dissipation capability in this region (Fig. 11(c)). Fig. 11(c) shows the fluid velocity distribution of the optimized microchannel. As the discrete cell can not be divided exactly by the calculated local w_{ch} and w_w. The redundant part in each discrete cell makes a channel with larger w_{ch}. The wider channel has a smaller flow resistance, resulting in larger flow rate and larger flow velocity. Therefore a certain part of the fluid in each discrete cell may 'leak' through the wide channel (Fig. 11(c)). This is one of the main error between the simulation results and the model (Fig. 12). And the structure considering the redundant part can be optimized further.

Fig. 12 shows the comparison of junction surface temperature between the optimized microchannel and the uniform microchannel in case B. Results show that the temperature uniformity of the optimized microchannel is apparently better than that of the uniform microchannel. In addition, the maximum temperature of the optimized microchannel is lower than the non-optimized one. The model calculated maximum surface temperature is 63 °C and the simulated maximum temperature is 65 °C. The model calculated surface temperature difference of optimized microchannel is only 13 °C, which is much smaller than that of the uniform microchannel 45 °C.

5. Conclusions

In this work, we presented a bi-layer compact thermal model for the microchannel with non-uniform heat source. It is based on the original 1D thermal resistance model of microchannel and the 3D thermal conduction model that describes the heat conduction in the solid layer is introduced. Therefore, the presented model takes the heat spreading effect in the solid layer into account and is more accurate for the surface temperature prediction of microchannels. Results calculated by this

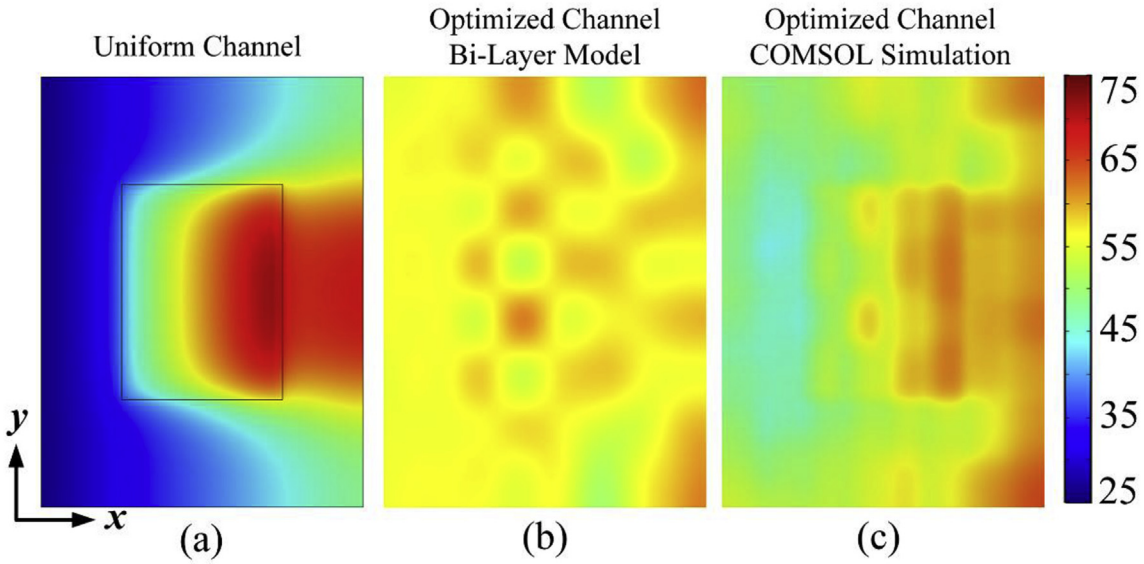

Fig. 12. (a) Simulated junction surface temperature for microchannel with uniform channels, (b) the bi-layer compact thermal model calculated junction surface temperature for optimized microchannel and (c) the simulated junction surface temperature for optimized microchannel.

model fit well with the COMSOL simulation and the error is within 4.8%. The surface temperature is mainly dependent on the heat flux, fluid temperature, convective thermal resistance in the convection layer and conduction thermal resistance in the solid layer. When the pumping power is set to be a constant, the flow rate, fluid temperature and convective thermal resistance are all determined by the channel width distribution. By optimizing the channel width distribution through using the genetic algorithm, we obtained the optimized microchannel structure. The optimized microchannel offers great surface temperature uniformity under the single phase liquid cooling condition with extremely non-uniform heat source. The junction surface temperature difference is reduced from 45 °C to 13 °C.

Acknowledgements

The authors would like to acknowledge the financial support by National Natural Science Foundation of China (51625601, 51576078, and 51606074), the Ministry of Science and Technology of the People´s Republic of China (Project No. 2017YFE0100600), the Financial support from Creative Research Groups Funding of Hubei Province (2018CFA001).

References

[1] J.B. Marcinichen, J.A. Olivier, J.R. Thome, On-chip two-phase cooling of datacenters: cooling system and energy recovery evaluation, Appl. Therm. Eng. 41 (2012) 36–51.
[2] X.B. Luo, R. Hu, S. Liu, K. Wang, Heat and fluid flow in high-power LED packaging and applications, Prog. Energ. Combust. Sci. 56 (2016) 1–32.
[3] R.C. Chu, R.E. Simons, M.J. Ellsworth, R.R. Schmidts, V. Cozzolino, Review of cooling technologies for computer products, IEEE T. Device Mat. Re. 4 (4) (2004) 568–585.
[4] V. Chiriac, S. Molloy, J. Anderson, K. Goodson, A Figure of Merit for Smart Phone Thermal Management, Electronics Cooling, 2015.
[5] B. Sun, H. Liu, Flow and heat transfer characteristics of nanofluids in a liquid-cooled CPU heat radiator, Appl. Therm. Eng. 115 (2017) 435–443.
[6] D.B. Tuckerman, R.F.W. Pease, High-performance heat sinking for VLSI, IEEE Electr. Device L. 2 (5) (1981) 126–129.
[7] L. Gong, J. Zhao, S. Huang, Numerical study on layout of micro-channel heat sink for thermal management of electronic devices, Appl. Therm. Eng. 88 (2015) 480–490.
[8] Y.T. Mu, L. Chen, Y.L. He, W.Q. Tao, Numerical study on temperature uniformity in a novel mini-channel heat sink with different flow field configurations, Int. J. Heat Mass Tran. 85 (2015) 147–157.
[9] C. Leng, X.D. Wang, T.H. Wang, W.M. Yan, Optimization of thermal resistance and bottom wall temperature uniformity for double-layered microchannel heat sink, Energ. Convers. Manage. 93 (2015) 141–150.
[10] X. Hao, B. Peng, G. Xie, Y. Chen, Efficient on-chip hotspot removal combined solution of thermoelectric cooler and mini-channel heat sink, Appl. Therm. Eng. 100 (2016) 170–178.
[11] J. Zhao, S. Huang, L. Gong, Z. Huang, Numerical study and optimizing on micro square pin-fin heat sink for electronic cooling, Appl. Therm. Eng. 93 (2016) 1347–1359.
[12] R. Chein, J. Chuang, Experimental microchannel heat sink performance studies using nanofluids, Int. J. Therm. Sci. 46 (2007) 57–66.
[13] J.M. Koo, S. Im, L. Jiang, K.E. Goodson, Integrated microchannel cooling for three-dimensional electronic circuit architectures, J. Heat Trans-T ASME 127 (2005) 49–58.
[14] H.Y. Zhang, D. Pinjala, T.N. Wong, K.C. Toh, Y.K. Joshi, Single-phase liquid cooled microchannel heat sink for electronic packages, Appl. Therm. Eng. 25 (2005) 1472–1487.
[15] T. Bello-Ochende, L. Liebenberg, J.P. Meyer, Constructal cooling channels for micro-channel heat sinks, Int. J. Heat Mass Tran. 50 (2007) 4141–4150.
[16] X.B. Luo, Z.M. Mao, Thermal modeling and design for microchannel cold plate with high temperature uniformity subjected to multiple heat sources, Int. Commun. Heat Mass 39 (2012) 781–785.
[17] A.C. Kheirabadi, D. Groulx, Cooling of server electronics: a design review of existing technology, Appl. Therm. Eng. 105 (2016) 622–638.
[18] S.V. Garimella, L.-T. Yeh, T. Persoons, Thermal management challenges in telecommunication systems and data centers, IEEE Trans. Compon. Packag. Manuf. Technol. 2 (2012) 1307–1316.
[19] J.R. Thome, State-of-the-art overview of boiling and two-phase flows in microchannel, Heat Tran. Eng. 27 (9) (2006) 4–19.
[20] T. Zhang, J.T. Wen, A. Julius, Y. Peles, M.K. Jensen, Stability analysis and maldistribution control of two-phase flow in parallel evaporating channels, Int. J. Heat Mass Tran. 54 (2011) 5298–5305.
[21] L. Cheng, G. Xia, Fundamental issues, mechanisms and models of flow boiling heat transfer in microscale channels, Int. J. Heat Mass Tran. 108 (2017) 97–127.
[22] H.J. Kwak, J.H. Kim, B.-S. Myung, M.H. Kim, D.E. Kim, Behavior of pool boiling heat transfer and critical heat flux on high aspect-ratio microchannels, Int. J. Therm. Sci. 125 (2018) 111–120.
[23] D. Lorenzini, C. Green, T.E. Sarvey, X. Zhang, Y. Hu, A.G. Fedorov, M.S. Bakir, Y. Joshi, Embedded single phase microfluidic thermal management for non-uniform heating and hotspots using microgaps with variable pin fin clustering, Int. J. Heat Mass Tran. 103 (2016) 1359–1370.
[24] C.S. Sharma, M.K. Tiwari, S. Zimmermann, T. Brunschwiler, G. Schlottig, B. Michel, D. Poulikakos, Energy efficient hotspot-targeted embedded liquid cooling of electronics, Appl. Energ. 138 (2015) 414–422.
[25] B. Shao, L. Wang, J. Li, H. Cheng, Multi-objective optimization design of a microchannel heat sink using adaptive genetic algorithm, Int. J. Numer. Method. H. 21 (3) (2011) 353–364.
[26] X.-H. Yang, S.-C. Tan, Y.-J. Ding, J. Liu, Flow and thermal modeling and optimization of micro/mini-channel heat sink, Appl. Therm. Eng. 117 (2017) 289–296.
[27] Z.M. Mao, X.B. Luo, S. Liu, Compact thermal model for microchannel substrate with high temperature uniformity subjected to multiple heat sources, Proc. IEEE 61th ECTC, Lake Buena Vista, FL, USA, 2011, pp. 1662–1672.
[28] C.S. Sharma, M.K. Tiwari, D. Poulikakos, A simplified approach to hotspot alleviation in microprocessors, Appl. Therm. Eng. 93 (2016) 1314–1323.
[29] S. Luhar, D. Sarkar, A. Jain, Steady state and transient analytical modeling of non-uniform convective cooling of a microprocessor chip due to jet impingement, Int. J. Heat Mass Tran. 110 (2017) 768–777.
[30] H.S. Carslao, J.C. Jaeger, Conduction of Heat in Solids, second ed., Clarendon Press, Oxford, 1959.
[31] R.V. Churchill, Fourier Series and Boundary Value Problems, McGraw Hill, 1941.
[32] G.L. Morini, Single-phase convective heat transfer in microchannels: a review of experimental results, Int. J. Therm. Sci. 43 (2004) 631–651.
[33] R.K. Shah, A.L. London, Laminar Flow Forced Convection in Ducts: a Source Book for Compact Heat Exchanger Analytical Data, Academic Press, 2014.
[34] R. Hu, T. Cheng, L. Li, J.L. Ma, X.B. Luo, Phosphor distribution optimization to decrease the junction temperature in white pc-LEDs by genetic algorithm, Int. J. Heat Mass Tran. 77 (2014) 891–896.
[35] H. Lee, D.D. Agonafer, Y. Won, F. Houshmand, C. Gorle, M. Asheghi, K.E. Goodson, Thermal modeling of extreme heat flux microchannel coolers for GaN-on-SiC semiconductor devices, J. Electron. Packag. 138 (2016) 010907.
[36] M.J. Madou, Fundamentals of Microfabrication: the Science of Miniaturization, second ed., CRC Press, Boca Raton, FL, 2002.